Research article

NMR IN BIOMEDICINE

Received: 25 August 2015, Revised: 19 November 2015, Accepted: 19 November 2015, Published online in Wiley Online Library: 11 January 2016

(wileyonlinelibrary.com) DOI: 10.1002/nbm.3466

Imaging the intratumoral–peritumoral extracellular pH gradient of gliomas

Daniel Coman[a,b]*, Yuegao Huang[a,b], Jyotsna U. Rao[a,b], Henk M. De Feyter[a,b], Douglas L. Rothman[a,b,c], Christoph Juchem[a,b,d] and Fahmeed Hyder[a,b,c]*

Solid tumors have an acidic extracellular pH (pH_e) but near neutral intracellular pH (pH_i). Because acidic pH_e milieu is conducive to tumor growth and builds resistance to therapy, simultaneous mapping of pH_e inside and outside the tumor (i.e., intratumoral-peritumoral pH_e gradient) fulfills an important need in cancer imaging. We used *B*iosensor *I*maging of *R*edundant *D*eviation in *S*hifts (BIRDS), which utilizes shifts of non-exchangeable protons from macrocyclic chelates (e.g., 1,4,7,10-tetraazacyclododecane-1,4,7,10-tetrakis(methylene phosphonate) or $DOTP^{8-}$) complexed with paramagnetic thulium (Tm^{3+}) ion, to generate *in vivo* pH_e maps in rat brains bearing 9L and RG2 tumors. Upon $TmDOTP^{5-}$ infusion, MRI identified the tumor boundary by enhanced water transverse relaxation and BIRDS allowed imaging of intratumoral-peritumoral pH_e gradients. The pH_e measured by BIRDS was compared with pH_i measured with ^{31}P-MRS. In normal tissue, pH_e was similar to pH_i, but inside the tumor pH_e was lower than pH_i. While the intratumoral pH_e was acidic for both tumor types, peritumoral pH_e varied with tumor type. The intratumoral–peritumoral pH_e gradient was much larger for 9L than RG2 tumors because in RG2 tumors acidic pH_e was found in distal peritumoral regions. The increased presence of Ki-67 positive cells beyond the RG2 tumor border suggested that RG2 was more invasive than the 9L tumor. These results indicate that extensive acidic pH_e beyond the tumor boundary correlates with tumor cell invasion. In summary, BIRDS has sensitivity to map the *in vivo* intratumoral–peritumoral pH_e gradient, thereby creating preclinical applications in monitoring cancer therapeutic responses (e.g., with pH_e-altering drugs). Copyright © 2016 John Wiley & Sons, Ltd.

Additional supporting information may be found in the online version of this article at the publisher's web site.

Keywords: metastasis; CEST; magnetic susceptibility; permeability; extravasation; SPIO

INTRODUCTION

Glioblastoma multiforme (GBMs) are the most lethal of brain cancers. In solid tumors, extracellular pH (pH_e) is more acidic than intracellular pH (pH_i) which is neutral to alkaline (1). An acidic pH_e seems to favor tumor growth and metastasis by activating matrix metalloproteases and cathepsins (2). Rapidly growing tumor cells possess elevated rates of glucose uptake but reduced rates of oxidative phosphorylation (i.e., Warburg effect), thereby causing acidity in the extracellular space (3). As acidic pH_e milieu is conducive to tumor cell propagation and builds resistance to therapy (4), imaging the pH_e gradient between inside and outside the tumor is an important unmet need in cancer imaging (5).

It has been shown that the acidic tumor microenvironment is related to the size and altered vascularity of tumors, which in turn stimulates hypoxia (6,7). Hypoxia induces gene expression changes that result in increased glycolysis and accumulation of carboxylic and lactic acids in the extracellular microenvironment. However, hypoxia is not the only contributor to acidification. Poor vascularity also hinders the elimination of protons and lactic acid contributing to a lower pH_e. A low pH_e increases metastatic potential, angiogenesis, induction of genomic instability and decreases immune function (8–11). A low pH_e also leads to resistance to radiotherapy and certain forms of chemotherapy (12). As proton movement across the cell membrane is coupled to the movement of other ions, pH_e is an important readout (13). Thus, quantitative and simultaneous mapping of pH_e inside and outside the tumor (i.e., intratumoral-peritumoral pH_e gradient) can be useful for tumor localization and following the response to cancer therapy (14).

* *Correspondence to: D. Coman and D. S. Fahmeed Hyder, N143 TAC (MRRC), 300 Cedar Street, Yale University, New Haven, CT 06520, USA. E-mail: daniel.coman@yale.edu; fahmeed.hyder@yale.edu*

a *D. Coman, Y. Huang, J. U. Rao, H. M. De Feyter, D. L. Rothman, C. Juchem, F. Hyder*
Magnetic Resonance Research Center, Yale University, New Haven, Connecticut, USA

b *D. Coman, Y. Huang, J. U. Rao, H. M. De Feyter, D. L. Rothman, C. Juchem, F. Hyder*
Radiology and Biomedical Imaging, Yale University, New Haven, Connecticut, USA

c *D. L. Rothman, F. Hyder*
Biomedical Engineering, Yale University, New Haven, Connecticut, USA

d *C. Juchem*
Neurology, Yale University, New Haven, Connecticut, USA

Abbreviations used: *APT, amide proton exchange; BIRDS, biosensor imaging of redundant deviation in shifts; CEST, chemical exchange saturation transfer; CSI, chemical shift imaging; DAB, diaminobenzidine; DOTP8-, 1,4,7,10-tetraazacyclododecane-1,4,7,10-tetrakis methylene phosphonate; FOV, field of view; FWHM, full width at half maximum; GFAP, glial fibrillary acidic protein; GBM, glioblastoma multiforme; H&E, hematoxylin and eosin; Pi, inorganic phosphate; MCT4, monocarboxylate transporter 4; PP, percentage of positive stained cells; PCr, phosphocreatine; SLR, Shinnar-Le Roux; SD, standard deviation; SS, staining score; SPIO, superparamagnetic iron oxide.*

Non-invasive MRI and MRS methods are mainstays for clinical cancer imaging (15). Smart MRI contrast agents enable physiochemical parameters like pH_e to be measured with lanthanide III ion (Ln^{3+}) derivatives of 1,4,7,10-tetraazacyclododecane (cyclen) (16), where most agents are built on the 1,4,7,10-tetraacetic acid (DOTA) backbone, similar to FDA-approved Gd^{3+} agents. While non-Gd^{3+} agents have yet to be tested in humans, molecular imaging with MRI has been demonstrated with a variety of DOTA-based macrocyclics in preclinical studies (17): relaxation-based methods and ***C**hemical **E**xchange **S**aturation **T**ransfer* (CEST). The relaxation-based methods rely on the paramagnetic effect induced by the Ln^{3+} ion on inner sphere of water protons, whereas CEST detects exchange between bulk water protons and an inner sphere of bound water that is shifted by the paramagnetic Ln^{3+} ion or exchangeable protons on the ligand (e.g., $-OH$ or $-NH_x$).

Recently, we established a method that combines high spatial resolution MRI with high molecular specificity MRS into a 3D chemical shift imaging (CSI) platform called ***B**iosensor **I**maging of **R**edundant **D**eviation in **S**hifts* (BIRDS), where paramagnetically-shifted non-exchangeable protons (i.e., $-CH_y$) on DOTA-based macrocyclic complexes are directly detected (18–24). Longitudinal (T_1) and transverse (T_2) relaxation times of non-exchangeable protons on BIRDS agents being very short (in ms range), allow high-resolution and high-speed CSI (18). BIRDS agents, similar to clinically-used DOTA, could potentially be translated across a range of magnetic fields because the T_2/T_1 ratio remains high and the proton shift sensitivities to the molecular event in the environment are largely unaffected. The readout of the physicochemical environment does not depend on diffusion or blood flow and BIRDS signals can be detected beyond MRI contrast (i.e., we see BIRDS signals when the MRI images are darkened by T_2 shortening) (18,19,21,22). Moreover, although the distribution of BIRDS agents may depend on vessel permeability (e.g., normal versus tumor tissue), the shift-based reporting is independent of the agent's concentration from voxel to voxel. Previously we showed that DOTA containing phosphonate agents (e.g., $TmDOTP^{5-}$ and $TmDOTA\text{-}4AmP^{5-}$) can provide pH_e maps with BIRDS (18,19).

In this study, we used BIRDS to measure pH_e in brains of 9L and RG2 tumor-bearing rats. We used $TmDOTP^{5-}$ because of its commercial availability, but other BIRDS agents can also be used. Specifically, our goal was to see whether BIRDS can help determine if tumor invasiveness can be mapped by the intratumoral–peritumoral pH_e gradient, defined as the absolute pH_e difference between values inside and outside the tumor.

MATERIALS AND METHODS

All experiments were performed according to NIH guidelines. Yale University's animal care and user committee (IACUC) approved the protocol. All scans were conducted on an 11.7 T Agilent (Santa Clara, CA, USA) horizontal-bore spectrometer with a bore size of 21 cm and maximum gradient strength of 400 mT/m, using ^1H and ^{31}P surface RF probes (each 1.4 cm diameter).

Animal preparation for rats bearing 9L and RG2 tumors

Adult male Fischer 344 rats (200–250 g; $n = 29$) were obtained from Yale University vendors and maintained according to approved animal care protocols. RG2 ($n = 16$) and 9L ($n = 13$) tumors were studied (25). Rats were anesthetized with isoflurane (2–3%) and positioned in a stereotaxic instrument with the incisor bar set at 3.0 mm below the interaural line. RG2 and 9L cells at high confluence were harvested, washed and suspended in appropriate media. Intrathalamic injections were made with a 25-μl Hamilton syringe, fitted with a 26-gauge beveled needle, into the right thalamus at coordinates 3 mm to the right from bregma and 3 mm ventral to the dura. A 5-μl volume of the cell suspension was injected over the course of 5 min and the needle was left in place for an additional 5 min before slow withdrawing. After injection, the scalp was closed, treated with antibiotic and a non-steroidal anti-inflammatory drug (meloxicam, 1 mg/kg) was injected subcutaneously to prevent pain and inflammation.

On the day of the scanning, rats were anesthetized with isoflurane (<2%), tracheotomized and artificially ventilated (70% N_2O/30% O_2). A femoral vein was cannulated (PE-10) to administer $TmDOTP^{5-}$ (0.4 mmol/kg). A femoral artery was cannulated (PE-50) for the monitoring of physiological parameters (pCO_2, pO_2, pH and blood pressure) throughout the experiment. An intraperitoneal line was inserted for administration of α-chloralose (40 mg/kg/h). α-Chloralose provides stable physiology over long periods for terminal rat experiments. However, for longitudinal experiments, isoflurane would be more ideal, but the exposure duration has to be kept short as the vasomotion effects are induced by prolonged exposure of this anesthetic. Because the body temperature decreases in animals under anesthesia, we used a water-heating pad to maintain the body temperature in the physiological range (36–37 °C).

The anesthetized rats were prepared with renal ligation (18,26) to maintain a high $TmDOTP^{5-}$ concentration gradient between the blood and extracellular space. As renal ligation stops clearance of the agent, with a slow infusion (~0.5 ml/h) of the agent (19), the agent concentration builds up in the microvasculature sufficiently high enough for slow extravasation, which subsequently leads to agent accumulation in the extracellular space. Based on prior observations in rats without renal ligation (27), we anticipated higher agent accumulation in tumors (vs. normal tissue) because of porous immature blood vessels. Fenestrated vessels in the circumventricular organ of the normal brain may also play a role in agent accumulation in the extracellular space (28–30). Previous ^{31}P MRS experiments in normal rats showed that the brain pH with and without renal ligation are similar (18,26). Ventilation was adjusted to maintain normal physiology. Body temperature was measured with a rectal temperature probe and no further adjustments in the water-heating pad were made for the entire duration of the experiment (~2 h). After the experiments, some rats were perfused and their brains were harvested for histopathological assessments.

Given that the relaxation rates of agents such as $TmDOTP^{5-}$ or $GdDOTA\text{-}4AmP^{5-}$ are possibly pH dependent (18,23,27), we directly measured the $TmDOTP^{5-}$ concentrations in normal and tumor tissues. A few rats ($n = 4$) were euthanized with focused microwave irradiation (31) and the brain tissue (i.e., normal and tumor) was removed, weighed and homogenized for agent concentration analysis *ex vivo* by ^1H NMR. Blood plasma samples were also collected to measure the agent in the plasma for correction of agent concentration in the tissue using tissue-plasma volumes (32). NMR solutions of each organ suspensions were prepared and 0.1 mM $TmDOTMA^-$ was used as an internal reference. NMR spectra were acquired using standard pulse-acquire experiments on an 11.7 T vertical bore magnet using short TR and resonance intensities of H6 proton of $TmDOTP^{5-}$ were measured. The final tissue concentrations of $TmDOTP^{5-}$ were calculated after reference and plasma corrections.

NMR IN BIOMEDICINE

Histological comparisons between 9L and RG2 tumors

Rats used for histochemical analysis were perfuse-fixed with 4% paraformaldehyde and embedded in paraffin. Brain tissue sections (4 μm) were stained with hematoxylin and eosin (H&E) for determination of the tissue structure followed by immunohistochemical stains for monocarboxylate transporter 4 (MCT4), glial fibrillary acidic protein (GFAP) and Ki-67. Immunostaining was performed as previously described (33). Primary antibody diluted in 0.1% BSA/PBS was applied for 90 min at room temperature for GFAP (1:500) (DAKO, Z0334) and MCT4 (1:50) (H-90, Santa Cruz Biotechnology, Santa Cruz, CA, sc-50329) and overnight at 4 °C for Ki-67 (1:100, Abcam, Cambridge, MA, ab66155). The sections were incubated with a goat anti-rabbit secondary antibody (1:500, Pierce Biotechnology, Rockford, IL, 31460) for 60 min followed by incubation with metal enhanced 3,3-diaminobenzidine (DAB; Pierce Biotechnology, Rockford, IL, 34065) for 10 min. The expression of various markers was quantified by evaluating the amount of DAB staining. The percentage of the positive-stained cells (PP) in each section was estimated by manually counting the cells as observed under ×50 magnification and graded in a scale ranging from 0% to 100%. The DAB color intensity (I_{DAB}) was graded as non-staining (0), faint (1), medium (2) and intense (3). The staining score (SS) representing the expression of the markers was defined as follows:

$$SS = I_{DAB} * PP \quad [1]$$

BIRDS for pH_e measurements

Prior to BIRDS experiments, spin-echo MRI datasets were obtained. Eleven coronal slices of 128 × 128 resolution and 1 mm thickness were acquired using a field of view (FOV) of 25 × 25 mm^2, a recycle time (TR) of 6 s and 12 different echo time (TE) values from 10 to 120 ms. The transverse relaxation time (T_2) and rate (R_2) maps were obtained in Matlab (MathWorks, Inc., Natick, MA, USA) by fitting the absolute MRI intensity versus TE to a single exponential function (34). After $TmDOTP^{5-}$ infusion, the same MRI data were acquired to compare the T_2 changes induced by the paramagnetic agent (27).

The *in vivo* CSI acquisition for BIRDS was optimized for a 3D sampling of 1 μl effective resolution, where the effective volume of a voxel was estimated by calculating the point spread function for Gaussian-weighted spherical encoding (21,35). A dual-banded refocused 90° Shinnar-Le Roux (SLR) RF pulse of 35 kHz bandwidth and 90 kHz separation with 205 μs duration was used for selective excitation of the H2/H3 and H6 protons of $TmDOTP^{5-}$. The datasets were acquired with a TR of 5 ms and an FOV of 25 × 25 × 25 mm^3. The phase encode gradient duration was 160 μs, the spectral window was 250000 Hz and the acquisition time was 4.1 ms. The ^{1}H spectrum for each encoding step was line broadened (300 Hz), phased (zero order) and baseline corrected (first order). The pH was calculated from the chemical shifts of the H2, H3 and H6 protons of $TmDOTP^{5-}$ (δ_2, δ_3 and δ_6) according to

$$pH = a_0 + \Sigma_{k=2,3,6}\, a_1^k \delta_k + \Sigma_{k=2,3,6}\, \Sigma_{j=2,3,6}\, a_2^{kj} \delta_k \delta_j \quad [2]$$

where the coefficients a_0, a_1^k and a_2^{kj} were calculated from linear least-squares fit of pH as a function of chemical shifts δ_2, δ_3 and δ_6, as previously described (18). The pH readout by Equation [2] is unaffected by $TmDOTP^{5-}$ concentration below 10 mM, which covers the $TmDOTP^{5-}$ concentration range we observed *in vivo* (18,26). Within the pH range of 6.6 to 7.6, the changes in the chemical shift for the H2, H3 and H6 protons at 35 °C are 4.3, 3.4 and 4.3 ppm, respectively.

^{31}P-MRS for pH_i measurements

Prior to BIRDS experiments, six glioma-bearing rats underwent single voxel ^{31}P-MRS acquisitions for intratumoral pH_i and peritumoral pH_i measurements, where the localized volumes were determined by the tumor size. ^{31}P spectra were acquired with ISIS localization (36) using a 1000 μs adiabatic half-passage pulse and the following acquisition parameters: TR = 16 s; the number of averages = 96; dummy scans = 16. The pH_i was calculated by

$$pH_i = pK_a + \log\left(\frac{\Delta\delta - \delta_1}{\delta_2 - \Delta\delta}\right) \quad [3]$$

where $\Delta\delta$ is the chemical shift difference between inorganic phosphate (P_i) and phosphocreatine (PCr) resonances, $\delta_1 = 3.23$ ppm and $\delta_2 = 5.70$ ppm are the corresponding chemical shift differences at low and high pH, respectively (35), and $pK_a = 6.915 \pm 0.002$ was calculated by linear least-squares regression of Pi-PCr data for the different conditions.

Analysis of pH_e maps

Regional variations of pH_e measured by BIRDS were assessed for voxels inside the tumor, at the tumor margin and well outside the tumor. The tumor margin was defined by MRI contrast. Intratumoral and peritumoral voxels were defined as all voxels inside and outside the tumor boundary defined by MRI, respectively. The voxels at the tumor margin were defined as one voxel that were either partly inside or outside of the tumor (i.e., right on the tumor boundary defined by MRI contrast). A parameter f that represents the fraction of voxels with pH values smaller than a threshold value pH_{th} was calculated and a sigmoidal function (describing a cumulative distribution) was used to fit f versus pH_{th} according to the equation:

$$f(pH < pH_{th}) = \frac{1}{1 + e^{-4S_{pH}(pH_{th} - pH_m)}} \quad [4]$$

where pH_m represents the distribution midpoints (given by pH_{th} value for which $f = 0.5$) while S_{pH} represents the slope of the sigmoidal curve at $pH_{th} = pH_m$.

Statistical analysis

All staining (Equation [1]) and pH_e (Equations [2],[3]) results were expressed as the mean ± standard deviation (SD) and comparisons were assessed by Student's t-test with two tails. Significance between pH_m measured intratumorally, within the tumor margin and peritumorally (Equation [4]) was assessed by Student's t-test, where P-values less than 0.05 were considered to be significant.

RESULTS

Figure 1 shows a comparison of histological stains for 9L and RG2 tumors. At the macroscopic scale, the H&E staining of both tumors showed a greater extent of hematoxylin staining (i.e., blue pigmentation) in the parenchyma (vs. parenchyma of normal brain tissue), which at the microscopic scale represented the tumoral mass within the inoculation zone (Fig. 1A).

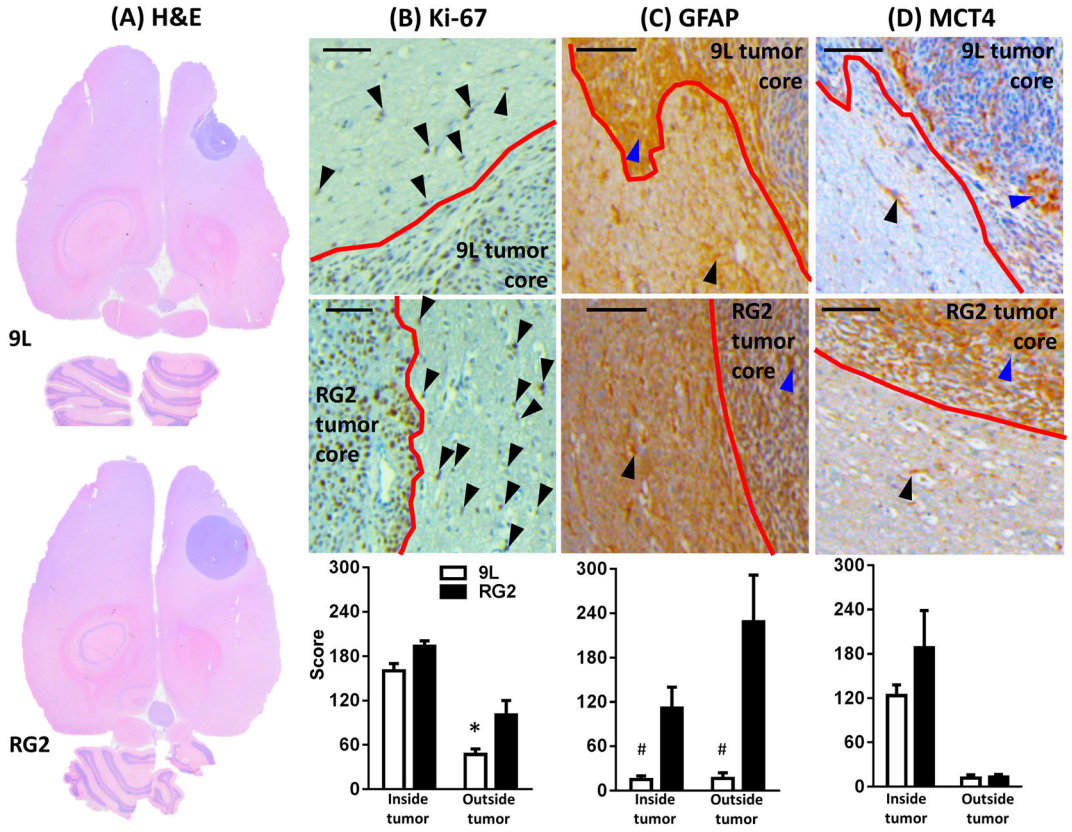

Figure 1. Evaluation of 9L and RG2 tumors by immunohistochemistry. Examples of staining results for (A) hematoxylin and eosin (H&E), (B) Ki-67, (C) GFAP and (D) MCT4 in individual rats. Black and blue arrows show positive diaminobenzidine (DAB) staining outside and inside the tumor boundary, respectively (scale bar =100 μm; red lines in B to D indicate the tumor boundary) for 9L (top) and RG2 (middle) tumors. Averaged staining scores (Equation [1]) inside and outside the tumor boundary (bottom) for a group of rats ($n = 3$ for each tumor type) are shown in graphs. Ki-67 expression outside the tumor core in RG2 was significantly higher than in 9L (*, $P < 0.031$); GFAP expression was higher in RG2 tumors than in 9L both inside and outside the tumor boundary (#, $P < 0.025$ and 0.027, respectively). While MCT4 staining was higher in RG2 tumors than 9L tumors, the difference did not reach significance.

The tumors were stained (Equation [1]) for markers of proliferation (Ki-67), gliosis (GFAP) and glycolysis/lactate transport (MCT4). Ki-67 (Fig. 1B) and MCT4 (Fig. 1D) showed nuclear and membrane localization, respectively. The higher expression of Ki-67 (Fig. 1B) and GFAP (Fig. 1C) was detected in cells beyond the RG2 tumor boundary. Increased expression of MCT4 and GFAP was observed in the RG2 tumor when compared with 9L, and both the 9L and RG2 tumors cells migrating from the tumor boundary showed MCT4 positive cells. Examples of immunohistochemistry images for Ki-67, GFAP and MCT4 in the same rat are shown in Supplementary Information Fig. S1, which is presented at different magnifications indicating locations of the images.

Supplementary information Figure S2 shows that MRI could identify the tumor with T_2 contrast upon $TmDOTP^{5-}$ infusion, similar to the Gd^{3+}-induced longitudinal relaxation time (T_1) contrast. Owing to the Tm^{3+}-induced paramagnetic effect, tumors could be identified either by darkening caused by the T_2 decrease (Supplementary information Fig. S2A) or R_2 enhancement (Supplementary information Fig. S2B) within the intratumoral regions in relation to peritumoral regions. The $TmDOTP^{5-}$-induced contrast in tumoral tissue is probably due to increased tumor vascular permeability allowing more $TmDOTP^{5-}$ in the extracellular space of tumors compared with neighboring tissue.

Figures 2A and 2B show representative BIRDS data from 9L- and RG2-bearing rats, respectively. The intratumoral regions of both tumors were localized similarly by T_2-based contrast. The intensities of $TmDOTP^{5-}$ protons were somewhat variable across different regions, with muscle signals being usually larger than those originating from the brain (Fig. 2Bii). As $TmDOTP^{5-}$ clearance rates from and permeability into various tissues are likely to be different, in some cases muscle and brain (i.e., both normal and tumor tissue) signal intensities were quite similar (Fig. 2Aii). While $TmDOTP^{5-}$ proton intensities varied across brain regions, only the shift variations of H2, H3 and H6 peaks allowed the pH to be determined independently of the agent concentration using Equation [2], thus enabling pH_e maps to be compared across all voxels both within and beyond the tumor boundary (Fig. 2Aiii and 2Biii). The intratumoral pH_e values were distinctly lower than peritumoral pH_e values. For example, in the 9L and RG2 tumors shown in Fig. 2Aiv and 2Biv the intratumoral pH_e values were 6.8 ± 0.1 and 6.7 ± 0.1, respectively, whereas a large majority of voxels in the peritumoral regions had pH_e values of 7.2 or higher. However, the brains with a RG2 tumor showed patterns of diffuse pH_e reductions several mm beyond the tumor boundary. In the brain with RG2 tumor shown the pH_e values were quite similar in the intratumoral regions vs. regions immediately adjacent to the tumor boundary, whereas in the brain with a 9L tumor shown the pH_e values were distinctly smaller in intratumoral regions vs. regions immediately adjacent to the tumor boundary.

Figure 3 shows a comparison of pH_e measured by BIRDS and pH_i measured using ^{31}P-MRS from the same animals bearing

NMR IN BIOMEDICINE

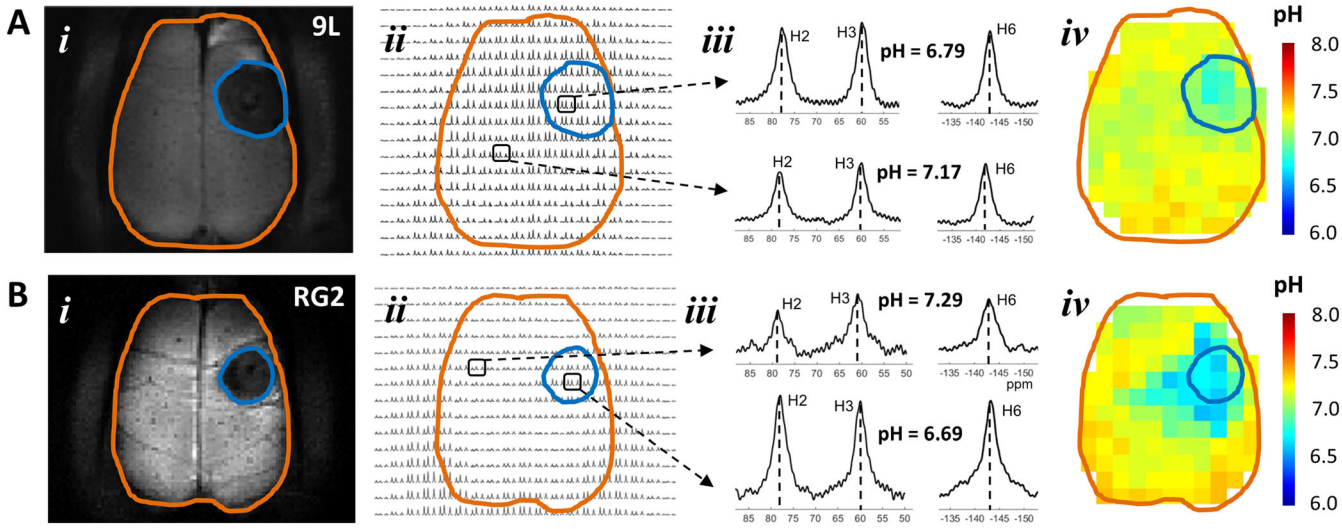

Figure 2. Representative pH_e maps from biosensor imaging of redundant deviation in shifts (BIRDS) data of rats bearing (A) 9L and (B) RG2 tumors. In (*i*) the T_2-weighted image shows the tumor localization identified by darkening (tumor = blue outline; brain = brown outline), which is likely due to increased tumor vascular permeability allowing more $TmDOTP^{5-}$ in the interstitial space of the tumor compared with neighboring non-tumor tissue (see Supplementary information Fig. S2). In (*ii*) a portion of the 3D chemical shift imaging (CSI) data for the slice in (*i*) shows varying $TmDOTP^{5-}$ levels throughout the brain. In (*iii*) examples of spectra from intratumoral and peritumoral voxels. In (*iv*) quantitative maps of pH_e were obtained using multiple $TmDOTP^{5-}$ peaks and their respective pH sensitivities (Equation [2]). (A) Specific voxels in a brain bearing 9L tumor shows significantly shifted $TmDOTP^{5-}$ peaks indicating different pH_e inside ($pH_e = 6.79$) than outside ($pH_e = 7.17$) the tumor boundary. The 9L tumor was identified by a significantly lower pH_e within the tumor boundary. (B) Specific voxels in a brain-bearing RG2 tumor shows significantly shifted $TmDOTP^{5-}$ peaks indicating different pH_e inside ($pH_e = 6.69$) than outside ($pH_e = 7.29$) the tumor boundary. The RG2 tumor was clearly identified by lower pH_e within the tumor boundary. While the most significantly low pH_e voxels were found inside the tumor margin, there were low pH_e voxels that were spread well beyond the tumor margin.

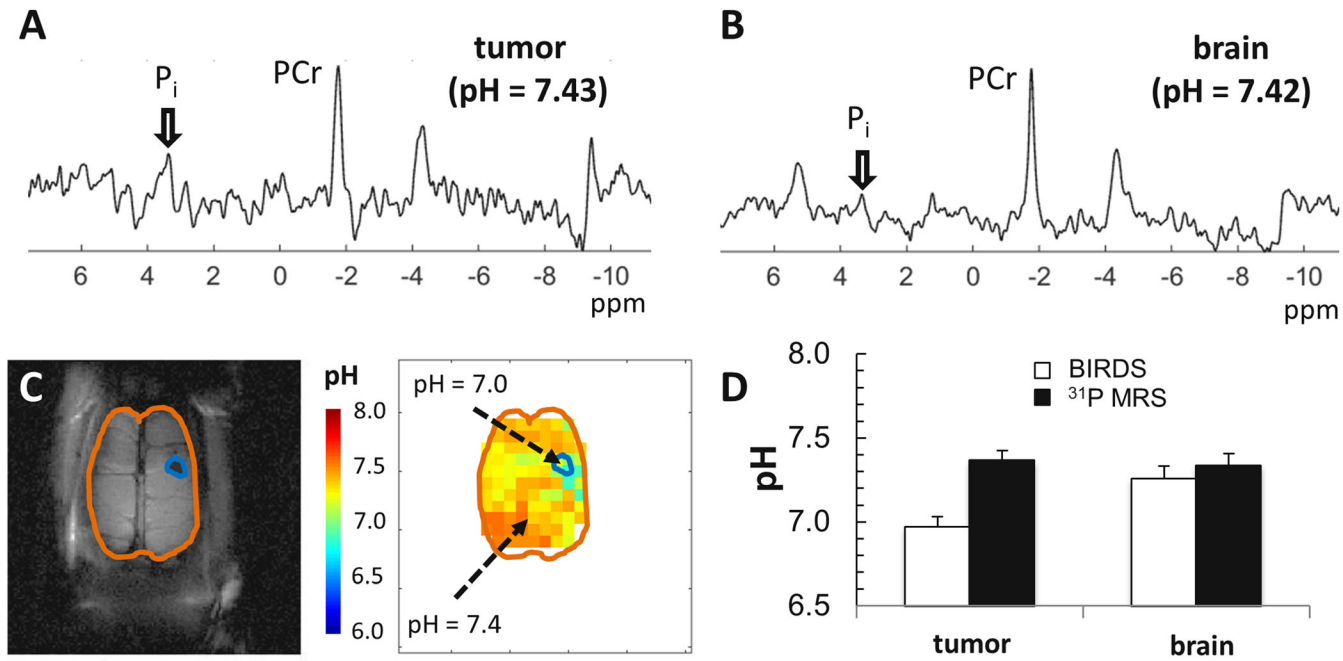

Figure 3. Comparison of pH measured by ^{31}P-MRS (pH_i) and biosensor imaging of redundant deviation in shifts (BIRDS) (pH_e) in small gliomas (~2 mm). The spectroscopic data were sequentially acquired in the same rats, first with ^{31}P-MRS and then with BIRDS. The pH measured by ^{31}P-MRS was calculated from the PCr and P_i shifts (Equation [3]), which reflects the intracellular compartment, whereas the pH measured by BIRDS (Equation [2]) represents the extracellular compartment. (A) ^{31}P spectrum from a voxel localized inside the tumor showed a pH value of 7.43. (B) ^{31}P spectrum from a voxel localized outside the tumor (i.e., inside normal brain tissue) showed a pH value of 7.42. (C) MRI and BIRDS data from the same rat, where the pH inside and outside the tumor were approximately 7.0 and 7.4, respectively. The tumor is indicated with the blue outline, whereas the brain is shown with brown outline. (D) Averaged pH measured by ^{31}P-MRS (black bars) and BIRDS (white bars) across a group of rats ($n = 6$). Good agreement was observed between pH_i (by ^{31}P-MRS) and pH_e (by BIRDS) in normal brain tissue ($P > 0.5$), whereas inside the tumor pH_i (by ^{31}P-MRS) was significantly higher than pH_e (by BIRDS). PCr, phosphocreatine; P_i, inorganic phosphate.

small gliomas. For BIRDS and ^{31}P-MRS, the pH-induced shifts are ~4 and ~1 ppm/pH unit, respectively, with a measurement error of < 0.01 pH units (18). ^{31}P spectra inside a tumor (Fig. 3A) and outside a tumor (Fig. 3B) show pH_i values that were neutral in both locations. In the same rat, after $TmDOTP^{5-}$ infusion, the BIRDS data show lower pH_e values inside vs. outside the tumor (Fig. 3C). Overall, there was good agreement between pH_i and pH_e in normal tissue outside the tumor, whereas inside the tumor pH_e was significantly lower than pH_i (Fig. 3D).

BIRDS had sufficient sensitivity to distinguish different sizes of 9L (Fig. 4) and RG2 (Fig. 5) tumors. However, in the case of small tumors (1–2 mm diameter) the partial contribution from the non-tumor tissue (based on tumor boundary defined by T_2-based contrast) could become significant. To minimize this contribution, for the intratumoral pH_e calculation we used only the voxels with a partial volume of more than 50% occupied by tumor tissue. Thus, we estimated the error in pH_e gradient between tumor and non-tumor tissue assuming a 50% partial volume for voxels positioned at the tumor boundary and a nominal pH_e gradient of 0.1 within each boundary voxel. As for small tumors (≤6 voxels) all voxels touch the boundary and experience partial volume effects, then the calculated error in pH_e gradient reported would be less than 0.05 units. In contrast, however, for larger tumors (40–50 voxels) only about 25% of the voxels touch the boundary and experience partial volume effects. Therefore, in larger tumors, the error in pH_e gradient estimation would be less than 0.013 units. As this suggests that the error in pH_e gradient between the tumor and its boundary scales inversely with the tumor size, we analyzed the larger 9L and RG2 tumors to find some differences in terms of intratumoral vs. peritumoral pH_e measurements. Overall, the intratumoral pH_e values of both tumor types became more acidic with tumor growth and changes in the peritumoral pH_e depended on the tumor type (i.e., more acidic peritumoral pH_e for tumors that invade).

For 9L tumors (Fig. 4), the distributions of peritumoral pH_e values in a small (Fig. 4A) and a large (Fig. 4B) tumor overlapped (e.g., 7.2–7.6), suggesting that the peritumoral pH_e is not significantly affected by 9L tumor growth. The distribution of intratumoral pH_e values in a large tumor (e.g., 6.7–7.2) was significantly shifted into acidic ranges compared with the intratumoral pH_e values in a small tumor (e.g., 7.0–7.2), suggesting that intratumoral pH_e becomes more acidic with 9L tumor growth.

For RG2 tumors (Fig. 5), the distributions of peritumoral pH_e values in a small (Fig. 5A) and a large (Fig. 5B) tumor overlapped but the spread was much larger than observed for 9L tumors (e.g., 6.8–7.6), suggesting that the peritumoral pH_e is already quite acidic in the earliest stages of RG2 tumor growth. The distribution of intratumoral pH_e values in a large tumor (e.g., 6.6–7.2) was significantly shifted into acidic ranges compared with the intratumoral pH_e values in a small tumor (e.g., 6.9–7.2), suggesting that the intratumoral pH_e becomes more acidic with RG2 tumor growth.

The intratumoral–peritumoral pH_e gradients (Fig. 6) measured by BIRDS were compared quantitatively. The sigmoidal relationships between pH_e thresholds and percentage of voxels with pH_e below these thresholds were represented by Equation [4]. For brains with 9L tumors (Fig. 6A) ~80% of intratumoral voxels had a pH_e lower than 7.0 (with values as low as 6.6) and ~80% of peritumoral voxels had a pH_e lower than 7.4 (with values as low as 7.1), whereas pH_e trends for voxels within the tumor boundary were in between these two other trends. For brains with RG2

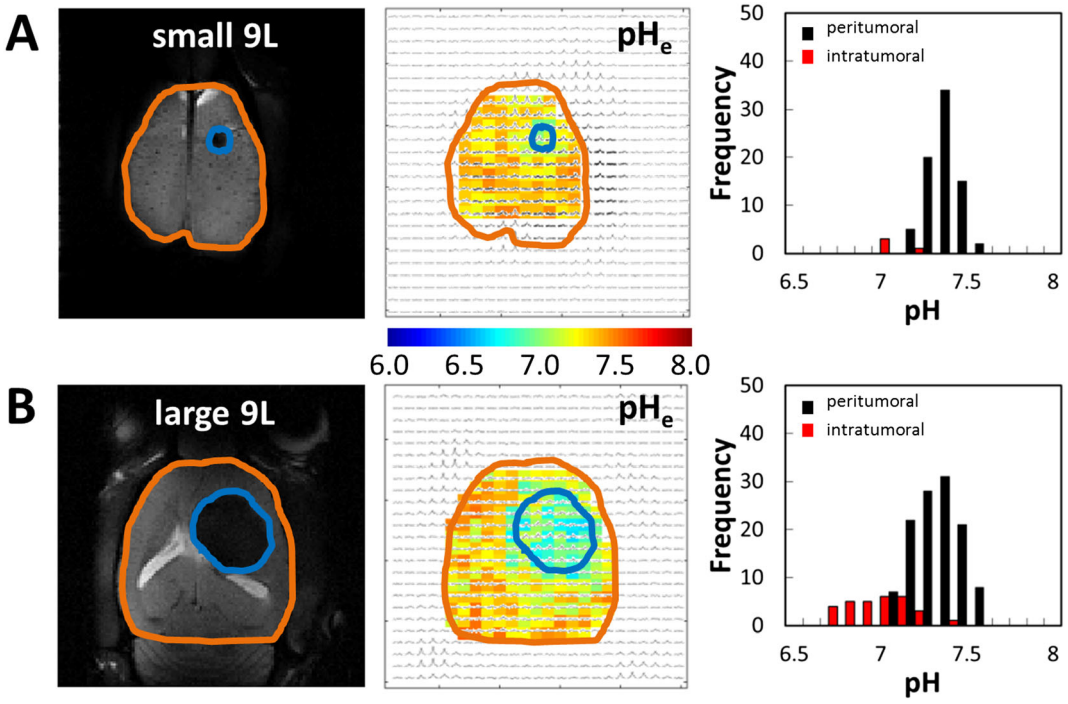

Figure 4. Representative biosensor imaging of redundant deviation in shifts (BIRDS) data from individual rats bearing 9L gliosarcomas of different sizes, shown in terms of pH_e maps and their respective histograms for values inside (intratumoral) and outside (peritumoral) the tumor. The MRI depiction of the tumor size is shown on the left (tumor = blue outline; brain = brown outline). (A) Data for a small 9L (~2 mm) shows that the pH_e were significantly separated for intratumoral voxels ($pH_e = 7.01 \pm 0.08$) and peritumoral voxels ($pH_e = 7.34 \pm 0.09$). (B) Data for a large 9L (~6 mm) shows also that the pH_e values were significantly separated for intratumoral voxels ($pH_e = 6.91 \pm 0.17$) and peritumoral voxels ($pH_e = 7.31 \pm 0.13$). The distributions of peritumoral pH_e values in small and large tumors were overlapping (e.g., 7.2–7.6). The distribution of intratumoral pH_e values in large tumor (e.g., 6.7–7.2) was significantly shifted into acidic ranges compared with the intratumoral pH_e values in small tumor (e.g., 7.0–7.2).

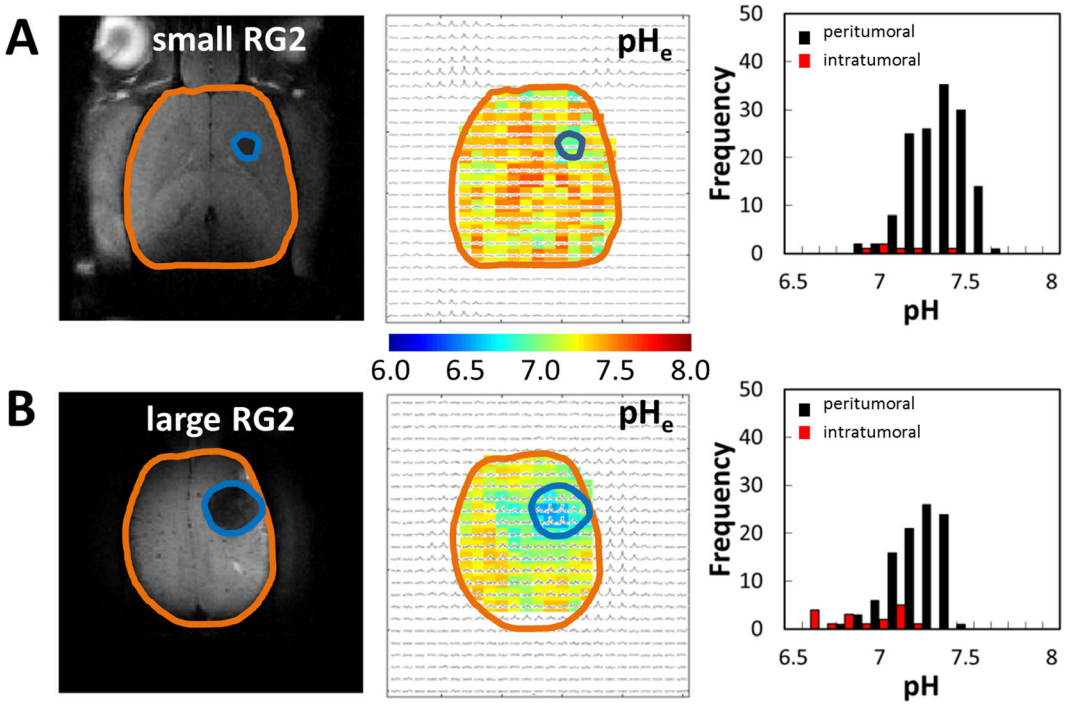

Figure 5. Representative biosensor imaging of redundant deviation in shifts (BIRDS) data from individual rats bearing RG2 gliomablastomas of different sizes, shown in terms of pH_e maps and their respective histograms for values inside (intratumoral) and outside (peritumoral) the tumor. The MRI depiction of the tumor size is shown on the left (tumor = blue outline; brain = brown outline). (A) Data for a small RG2 (~2 mm) shows that the pH_e were significantly separated for intratumoral voxels ($pH_e = 6.84 \pm 0.22$) and peritumoral voxels ($pH_e = 7.31 \pm 0.16$). (B) Data for a large RG2 (~5 mm) shows also that the pH_e values were significantly separated for intratumoral voxels ($pH_e = 6.91 \pm 0.17$) and peritumoral voxels ($pH_e = 7.18 \pm 0.14$). The distributions of peritumoral pH_e values in small and large tumors were overlapping but the spread was quite large (e.g., 6.8–7.6). The distribution of intratumoral pH_e values in large tumor (e.g., 6.6–7.2) was significantly shifted into acidic ranges compared to the intratumoral pH_e values in small tumor (e.g., 6.9–7.2).

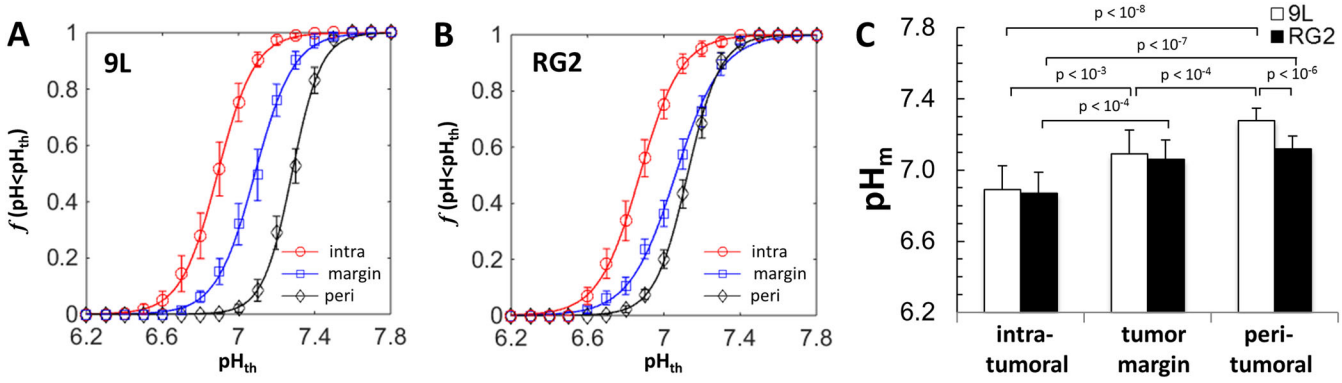

Figure 6. The intratumoral-peritumoral pH_e gradient measured by biosensor imaging of redundant deviation in shifts (BIRDS) for 9L ($n = 13$) and RG2 ($n = 16$) tumors. Quantitative variations of pH_e were obtained for intratumoral voxels (red circles), voxels within the tumor margin (blue squares), and peritumoral voxels (black diamonds). In (A) and (B) the vertical axis is a parameter f that represents the fraction of voxels with pH_e values smaller than a threshold value (pH_{th}), which is indicated on the horizontal axis. Variations of pH_e for 9L and RG2 tumors show sigmoidal relationships for all voxels. The data points are the average, the error bars are the standard error, and the lines are the non-linear fit of f to Equation [4] for intratumoral voxels (red line), voxels within the tumor margin (blue line), and peritumoral voxels (black line). (A) For 9L tumors, pH_e values of the margin were significantly different from peritumoral and intratumoral pH_e values. (B) For RG2 tumors, pH_e values of the margin were not significantly different from peritumoral pH_e values, but significantly different from intratumoral pH_e values. (C) The overall pH_e differences between 9L and RG2 tumors are shown with regard to the distribution midpoint pH_m, which represents the pH_e at $f = 0.5$. Statistical group comparison using Student's t-test with two tails for pH_e shows that pH_m was significantly different for 9L ($P < 0.001$) for all three possible comparisons (intratumoral vs. margin, peritumoral vs. margin, and intratumoral vs. peritumoral), while for RG2 was significantly different ($P < 0.0001$) only for intratumoral vs. margin and intratumoral vs. peritumoral comparisons. When comparing pH_m values for 9L versus RG2, only the peritumoral regions showed significant differences ($P < 10^{-6}$).

tumors (Fig. 6B) ~80% of intratumoral voxels had a pH_e lower than 7.0 (with values as low as 6.6) and ~80% of peritumoral voxels had a pH_e lower than 7.3 (with values as low as 6.8), whereas pH_e trends for voxels within the tumor boundary nearly matched pH_e trends for peritumoral voxels. Hence, for 9L tumors the peritumoral pH_e was clearly separated from intratumoral pH_e and pH_e within the tumor boundary (Fig. 6C). However, in RG2 tumors the peritumoral pH_e was only clearly separated from

the intratumoral pH_e because the peritumoral pH_e was quite similar to pH_e within the tumor boundary (Fig. 6C). These results indicate a significantly steeper intratumoral–peritumoral pH_e gradient for brains with 9L tumors compared with brains bearing RG2 tumors (i.e., ~0.4 vs. ~0.2; Fig. 6C). The histograms summarizing these results in terms of pH_e distribution measured by BIRDS for intratumoral, margin and peritumoral regions for 9L and RG2 tumors are shown in Supplementary information Fig. S3. The most probable pH_e values and the full width at half maximum (FWHM) obtained from a Gaussian fit of the distribution are given in Table 1. As expected, for both 9L and RG2 tumors, the most probable pH_e values obtained from the Gaussian fit of the pH_e distribution (Supplementary information Fig. S3 and Table 1) were the same (within the estimated error of the fit) as the distribution midpoints pH_m obtained from the sigmoidal fit (Fig. 6), indicating that both types of analysis gave the same result.

DISCUSSION

Because acidic pH_e is believed to facilitate tumor cell invasion (2), quantitating pH_e could have significant implications for the diagnosis of tumor invasiveness and the response to therapy (14,37). As most MRI-based molecular imaging methods focus on the intratumoral pH_e (27,38,39), the need for mapping the intratumoral–peritumoral pH_e gradient has escaped attention. Thus, we used BIRDS to measure the intratumoral–peritumoral pH_e gradient in rat brains bearing 9L and RG2 tumors to assess how this parameter changes with tumor invasiveness.

Pros and cons of molecular imaging with BIRDS

BIRDS is a molecular imaging platform that detects paramagnetically-shifted non-exchangeable protons on the agent as opposed to water proton relaxation, which is the norm in molecular imaging with MRI. Because a paramagnetic CEST agent also has non-exchangeable protons, these CEST agents also show BIRDS properties and allow dual modality with the same agent (20,23). BIRDS is compatible with superparamagnetic iron oxide (SPIO) and the pH_e readouts from BIRDS are unaffected by high-dose SPIO (40), because the linewidths of $TmDOTP^{5-}$ resonances in rat brain are already large (1–2 ppm) and they do not change significantly after SPIO addition. Therefore, it should be possible to apply SPIO nanoparticles to monitor drug delivery by MRI and then use BIRDS to monitor the physicochemical effects (e.g., pH_e) of the drugs delivered.

Signal of agents like $TmDOTP^{5-}$ and $TmDOTMA^{-}$ can be observed in the brain of rats that have undergone renal ligation even after several hours following the start of the infusion (19), suggesting slow clearance from the extracellular space. We previously measured the presence of $TmDOTP^{5-}$ in the cerebral spinal fluid (26). We proposed that the fenestrated vessels of circumventricular organs may also provide an additional route for these agents to gain access to the extracellular space because fenestrated vessels in this location are present even in the adult brain (28–30). Additionally, using ^{1}H MRS, at the end of 2 h of infusion, we measured the $TmDOTP^{5-}$ concentration in blood to be ~3 mM, whereas in extracted tissues from normal and tumor regions the $TmDOTP^{5-}$ concentrations were ~0.2 and ~0.5 mM, respectively. These signals contain ~13% contribution from blood (3% partial volume) and ~87% from extracellular space (20% partial volume) (18,19,26). Owing to lack of reports on the volumes of extracellular and intravascular spaces in brain tumors, we assumed that the fractions of these compartments inside and outside tumors are the same. Thus, $TmDOTP^{5-}$ in the extracellular space of normal and tumor tissues was ~0.5 mM and ~2 mM, respectively.

Protonation/deprotonation of phosphonate groups of $DOTP^{8-}$ or $DOTA\text{-}4AmP^{8-}$ is fast on the NMR timescale, which can be observed either by the pH-dependent variations of the H2, H3 and H6 chemical shifts with BIRDS (18) or relaxation MRI (27). Thus, protonation/deprotonation of $TmDOTP^{5-}$ or other agents such as $GdDOTA\text{-}4AmP^{5-}$ is not diffusion limited in free solution, but it might be affected in normal or tumor tissue owing to different water diffusion environments. However, even for regions with restricted (slow) water diffusion, we and others expect that the protonation/deprotonation equilibrium is reached rapidly because $TmDOTP^{5-}$ (or $GdDOTA\text{-}4AmP^{5-}$) is a small molecule and is dilute in an otherwise aqueous medium (18,27). Moreover, *in vitro* BIRDS measurements with large temperature variations do not affect the pH readout capability of $DOTP^{8-}$ (or $DOTA\text{-}4AmP^{8-}$) (18,23), suggesting that the pH_e measured with such probes represent protonation/deprotonation equilibrium over the observed diffusion range *in vivo*. However, future studies with ADC and high-resolution BIRDS may indicate possible correlation (or lack thereof) between pH_e and water diffusion.

The paramagnetic effect of $TmDOTP^{5-}$ on water protons provides sufficient T_2 contrast for identification of the intratumoral volume, similar to enhanced T_1 contrast with Gd^{3+} agents for tumor detection (26,27). As suggested by Martinez *et al.* (27) and others (26), a greater extent of these agents' extravasation across porous tumor blood vessels is responsible for the superior MRI contrast between the tumor and surrounding tissue (Supplementary information Fig. S2). In addition, detection of the paramagnetically-shifted $TmDOTP^{5-}$ protons with BIRDS allows physicochemical imaging of the brain (Fig. 2).

While the current study used $TmDOTP^{5-}$ for pH detection with BIRDS, in future studies methyl groups can be added in select regions of the ligand to improve sensitivity, thereby allowing reduced CSI voxel sizes and/or decreasing the amount of agent dose needed. At present, 1 μl voxel size in 3D CSI of the whole brain is acquired in ~10 min with a minimum of ~0.2 mmol/kg dose using methylated agents (e.g., $TmDOTMA^{-}$) for a nominal signal-to-noise ratio (21,22). In addition, preliminary results in our laboratory towards avoiding surgical intervention used to raise plasma levels of the agent (18,19), show that it is possible to co-infuse intravenously the agent with drugs that temporarily inhibit renal excretion (e.g., probenecid is used in humans to raise plasma concentration of drugs) (41). The co-infusion of the agent and probenecid should also lower the agent dose and allow repeated scans for longitudinal studies.

Table 1. Most probable pH_e values and the full width at half maximum (FWHM) obtained from the fit of the normal (Gaussian) distribution versus pH_e shown in Supplementary information Fig. S3 for intratumoral, margin and peritumoral regions in the 9L and RG2 tumors.

Region	9L		RG2	
	pH_e	FWHM	pH_e	FWHM
intratumoral	6.90 ± 0.01	0.38 ± 0.01	6.87 ± 0.01	0.44 ± 0.02
tumor margin	7.09 ± 0.01	0.41 ± 0.02	7.08 ± 0.01	0.50 ± 0.03
peritumoral	7.29 ± 0.01	0.32 ± 0.02	7.13 ± 0.01	0.35 ± 0.01

NMR IN BIOMEDICINE

Morphology of 9L and RG2 tumors

Syngenic rat brain tumor models are widely used in preclinical cancer research (25). 9L and RG2 are considered gliosarcoma and glioblastoma models, respectively. A distinct advantage of such syngeneic models is that they are grafted into fully immune competent rats. 9L tumor margins are sharply delineated with little obvious invasion into the contiguous normal brain. The RG2 glioma has a relatively more infiltrative growth with foci of local collective invasion (25). 9L and RG2 tumors have different metabolite profiles and differences in energy demand (42). Microvessel density and angiogenesis seem to be higher in RG2 when compared with 9L by histological studies; however, MRI methods could not reveal these differences (43).

Higher Ki-67 staining was detected in cells beyond the RG2 tumor boundary (Fig. 1B) in agreement with prior observations (44). In addition, RG2 showed significantly higher GFAP (Fig. 1C) and MCT4 (Fig. 1D) staining inside the tumor compared with 9L, while significantly higher GFAP staining was observed outside the tumor in RG2 when compared with 9L. These results collectively imply morphological differences between 9L and RG2, where RG2 tumor cells seem to invade beyond the tumor boundary more than 9L tumor cells.

pH_e mapping in tumors

Various factors contribute to the acidity of the extracellular space in peritumoral and intratumoral regions. It is generally believed that the Warburg effect mediates the acidosis within the tumor core while beyond the tumor core inflammatory responses by lymphocytes and macrophage infiltrations could certainly affect pH_e. However, it should be noted that poor perfusion in tumors hampers the ability of the microenvironment to remove tumor-derived acid through diffusion into blood vessels. Thus, H^+ ions and lactic acid generated as a result of the tumoral Warburg effect can diffuse through the interstitial space along the concentration gradient owing to the lack of effective clearance by blood flow (45).

The low intratumoral pH_e values in gliomas measured here are similar to prior MRI/MRS reports (27,46). We compared pH_e measured by BIRDS with pH_i measured by ^{31}P-MRS. In both tumors, intratumoral pH_e from BIRDS was significantly lower (~6.9) compared with intratumoral pH_i from ^{31}P-MRS (~7.4) and peritumoral pH_e approached peritumoral pH_i (Fig. 3). In agreement with prior observations (1,14), our results indicate that the intratumoral pH_e-pH_i gradient is large, whereas the peritumoral pH_e-pH_i gradient is negligible. However, the intratumoral–peritumoral pH_e gradient was much smaller for brains bearing RG2 vs. 9L tumors, indicating tumor invasion relates to diffuse areas of low pH_e (Fig. 6).

A good example of pH_e measurement in brain tumors is by Martinez *et al.*, where they used a pH-sensitive T_1 agent GdDOTA-4AmP^{5-} injected intravenously into rats with C6 tumors with a pH-insensitive T_2 agent DyDOTP^{5-} (27). The T_2 change caused by DyDOTP^{5-}, similar to T_2 darkening we observed with TmDOTP^{5-} in this study (Supplementary information Fig. S2), allowed [Gd^{3+}] estimation to convert the T_1 change of GdDOTA-4AmP^{5-} into pH_e. Alternate MRI methods using CEST, with either diamagnetic or paramagnetic agents (47), provide relative estimates of intratumoral pH_e. Diamagnetic CEST has detected enhanced amide proton exchange (APT) in brain tumors (38,48), where the APT is related to pH_i. Diamagnetic CEST has been applied for other types of tumors with a low intratumoral pH_e (39).

As the focus in all previously reported pH-dependent maps with MRI and CEST methods was on intratumoral pH_e, the intratumoral-peritumoral pH_e gradient had not been quantitatively determined. Peritumoral pH_e mapping has not received attention in past studies, and hence, in the absence of such data it could be inherently assumed that peritumoral pH_e is close to normal tissue pH_e. In this study, we tested this assumption in two different tumor types and we showed that the peritumoral pH_e of an aggressive tumor (RG2) is more acidic than the normal tissue pH_e. The MRI-measured intratumoral pH_e reported by GdDOTA-4AmP^{5-} for C6 tumors (27) is in general agreement with BIRDS-measured intratumoral pH_e reported by TmDOTP^{5-} for 9L and RG2 tumors. However, in the present study we were able to compare the peritumoral pH_e with intratumoral pH_e. The ability to compare the intratumoral–peritumoral pH_e gradient may be an important distinction as the diffuse nature of pH_e reductions beyond the tumor boundary has been linked to tumor invasiveness (i.e., RG2 has the higher extent of Ki-67 positive cells beyond the tumor boundary). These results are in good agreement with past studies, using primarily MRS techniques, that have shown that the intratumoral–peritumoral pH_e gradient varies with tumor type [for a recent review see (2)].

CONCLUSION

Our results show that intratumoral–peritumoral pH_e gradient mapping by BIRDS can be used for high-resolution spatial evaluation of the tumor microenvironment. While the acidic intratumoral pH_e is a target for various cancer drugs (49), future chemotherapies could be further targeted to the diffuse areas of low peritumoral pH_e because tumor cells invade (50).

Targeting the acidic pH_e of the tumor microenvironment provides several therapeutic options. The proton pump seems to be a successful target for inhibitor designs to change the intratumoral pH_e. For example, the V-ATPase inhibitor bafilomycin A1 inhibits tumor growth by increasing the intratumoral pH_e without perturbing the intratumoral pH_i (51). Another approach for increasing intratumoral pH_e is systemic buffering by sodium bicarbonate and/or trisodium citrate (52,53).

Overall, a combination of pH-regulating drugs with other cancer treatments (e.g., targeting glycolysis, chemotherapy and/or radiation) might help to reduce the tumor growth or prevent metastasis. One such example is the bicarbonate approach combined with dichloroacetate, which increases pyruvate dehydrogenase flux (52). In any event, if we can spatially localize the regions of low pH_e, both within and beyond the tumor margin, we may detect tumor invasion, proliferation, angiogenesis and the response to therapy to determine the prognosis of the disease.

Acknowledgements

Supported by NIH grants (R01 EB-011968, R01 CA-140102 and P30 NS-052519).

AUTHOR CONTRIBUTIONS

D.C., Y.H., F.H. designed research. D.C., Y.H., J.U.R., H.M.D.F., C.J., F.H. performed research. D.C., Y.H., J.U.R., F.H. analyzed data. D.C., Y.H., J.U.R., D.L.R., F.H. wrote the paper.

DISCLOSURE/CONFLICT OF INTEREST

The authors declare that there are no conflicts of interest.

REFERENCES

1. Gerweck LE. The pH difference between tumor and normal tissue offers a tumor specific target for the treatment of cancer. Drug Resist. Updat. 2000; 3(1): 49–50.
2. Hashim AI, Zhang X, Wojtkowiak JW, Martinez GV, Gillies RJ. Imaging pH and metastasis. NMR Biomed. 2011; 24(6): 582–591.
3. Gatenby RA, Gillies RJ. Why do cancers have high aerobic glycolysis? Nat. Rev. Cancer 2004; 4(11): 891–899.
4. Webb BA, Chimenti M, Jacobson MP, Barber DL. Dysregulated pH: a perfect storm for cancer progression. Nat. Rev. Cancer 2011; 11(9): 671–677.
5. Kalpathy-Cramer J, Gerstner ER, Emblem KE, Andronesi OC, Rosen B. Advanced magnetic resonance imaging of the physical processes in human glioblastoma. Cancer Res. 2014; 74(17): 4622–4637.
6. Raghunand N, Gatenby RA, Gillies RJ. Microenvironmental and cellular consequences of altered blood flow in tumours. Br. J. Radiol. 2003 76 Spec No; 1: S11–S22.
7. Wachsberger P, Burd R, Dicker AP. Tumor response to ionizing radiation combined with antiangiogenesis or vascular targeting agents: exploring mechanisms of interaction. Clin. Cancer Res. Off J. Am. Assoc. Cancer Res 2003; 9(6): 1957–1971.
8. Lardner A The effects of extracellular pH on immune function. J. Leukoc. Biol. 2001; 69(4): 522–530.
9. Martinez-Zaguilan R, Seftor EA, Seftor RE, Chu YW, Gillies RJ, Hendrix MJ. Acidic pH enhances the invasive behavior of human melanoma cells. Clin. Exp. Metastasis 1996; 14(2): 176–186.
10. Morita T, Nagaki T, Fukuda I, Okumura K. Clastogenicity of low pH to various cultured mammalian cells. Mutat. Res. 1992; 268(2): 297–305.
11. Shi Q, Le X, Wang B, Abbruzzese JL, Xiong Q, He Y, Xie K. Regulation of vascular endothelial growth factor expression by acidosis in human cancer cells. Oncogene 2001; 20(28): 3751–3756.
12. Song CW, Griffin R, Park HJ. Influence of tumor pH on therapeutic response. In *Cancer Drug Resistance*, Teicher B (ed.). Humana Press: New York, USA, 2006; 21–42.
13. Honasoge A, Sontheimer H. Involvement of tumor acidification in brain cancer pathophysiology. Front. Physiol. 2013; 4: 316.
14. Gillies RJ, Raghunand N, Garcia-Martin ML, Gatenby RA. pH imaging. A review of pH measurement methods and applications in cancers. IEEE Eng. Med. Biol. Magnesium 2004; 23(5): 57–64.
15. Bhujwalla ZM, Artemov D, Ballesteros P, Cerdan S, Gillies RJ, Solaiyappan M. Combined vascular and extracellular pH imaging of solid tumors. NMR Biomed. 2002; 15(2): 114–119.
16. Hingorani DV, Bernstein AS, Pagel MD. A review of responsive MRI contrast agents: 2005–2014. Contrast Media Mol. Imaging 2014. DOI:10.1002/cmmi.1629.
17. Yoo B, Pagel MD. An overview of responsive MRI contrast agents for molecular imaging. Front. Biosci. 2008; 13: 1733–1752.
18. Coman D, Trubel HK, Rycyna RE, Hyder F. Brain temperature and pH measured by ^{1}H chemical shift imaging of a thulium agent. NMR Biomed. 2009; 22(2): 229–239.
19. Coman D, Trubel HK, Hyder F. Brain temperature by Biosensor Imaging of Redundant Deviation in Shifts (BIRDS): Comparison between TmDOTP5- and TmDOTMA-. NMR Biomed. 2010; 23(3): 277–285.
20. Coman D, Kiefer GE, Rothman DL, Sherry AD, Hyder F. A lanthanide complex with dual biosensing properties: CEST (chemical exchange saturation transfer) and BIRDS (biosensor imaging of redundant deviation in shifts) with europium DOTA-tetraglycinate. NMR Biomed. 2011; 24(10): 1216–1225.
21. Coman D, de Graaf RA, Rothman DL, Hyder F. In vivo 3D molecular imaging with BIRDS at high spatiotemporal resolution. NMR Biomed. 2013; 26(11): 1589–1595.
22. Coman D, Sanganahalli BG, Jiang L, Hyder F, Behar KL. Distribution of temperature changes and neurovascular coupling in rat brain following 3,4-methylenedioxymethamphetamine (MDMA,'ecstasy') exposure. NMR Biomed. 2015; 28(10): 1257–1266.
23. Huang Y, Coman D, Ali MM, Hyder F. Lanthanide ion (III) complexes of 1,4,7,10-tetraazacyclododecane-1,4,7,10-tetraaminophosphonate for dual biosensing of pH with chemical exchange saturation transfer (CEST) and biosensor imaging of redundant deviation in shifts (BIRDS). Contrast Media Mol. Imaging 2015; 10(1): 51–58.
24. Huang Y, Coman D, Hyder F, Ali MM. Dendrimer-based Responsive MRI Contrast Agents (G1-G4) for Biosensor Imaging of Redundant Deviation in Shifts (BIRDS). Bioconjug. Chem. 2015.
25. Barth RF, Kaur B. Rat brain tumor models in experimental neuro-oncology: the C6, 9L, T9, RG2, F98, BT4C, RT-2 and CNS-1 gliomas. J. Neurooncol 2009; 94(3): 299–312.
26. Trubel HK, Maciejewski PK, Farber JH, Hyder F. Brain temperature measured by 1 H-NMR in conjunction with a lanthanide complex. J. Appl. Physiol. 2003; 94(4): 1641–1649.
27. Martinez GV, Zhang X, Garcia-Martin ML, Morse DL, Woods M, Sherry AD, Gillies RJ. Imaging the extracellular pH of tumors by MRI after injection of a single cocktail of T1 and T2 contrast agents. NMR Biomed. 2011; 24(10): 1380–1391.
28. Yoshida Y, Yamada M, Wakabayashi K, Ikuta F. Endothelial fenestrae in the rat fetal cerebrum. Brain Res. Dev. Brain Res. 1988; 44(2): 211–219.
29. Kaya M, Chang L, Truong A, Brightman MW. Chemical induction of fenestrae in vessels of the blood–brain barrier. Exp. Neurol. 1996; 142(1): 6–13.
30. Johnson AK, Gross PM. Sensory circumventricular organs and brain homeostatic pathways. FASEB J. 1993; 7(8): 678–686.
31. de Graaf RA, Chowdhury GM, Brown PB, Rothman DL, Behar KL. In situ 3D magnetic resonance metabolic imaging of microwave-irradiated rodent brain: a new tool for metabolomics research. J. Neurochem. 2009; 109(2): 494–501.
32. Lasher EP, Simmons BS, Everett NB. Effects of semistarvation on the distribution of erythrocytes and plasma in organs and tissues of the rat. J. Nutr. 1958; 65(2): 317–326.
33. van Berkel A, Rao JU, Kusters B, Demir T, Visser E, Mensenkamp AR, van der Laak JA, Oosterwijk E, Lenders JW, Sweep FC, Wevers RA, Hermus AR, Langenhuijsen JF, Kunst DP, Pacak K, Gotthardt M, Timmers HJ. Correlation Between In Vivo 18F-FDG PET and Immunohistochemical Markers of Glucose Uptake and Metabolism in Pheochromocytoma and Paraganglioma. J. Nucl. Med. Off. Publ. Soc. Nucl. Med 2014; 55(8): 1253–1259.
34. Strohbehn G, Coman D, Han L, Ragheb RR, Fahmy TM, Huttner AJ, Hyder F, Piepmeier JM, Saltzman WM, Zhou J. Imaging the delivery of brain-penetrating PLGA nanoparticles in the brain using magnetic resonance. J. Neurooncol 2015; 121(3): 441–449.
35. de Graaf RA In *vivo NMR Spectroscopy - Principles and Techniques*, 2nd edn. Wiley, John & Sons, Incorporated: Chichester, 2007.
36. Ordidge RJ, Connelly A, Lohman JAB. Image-selected in Vivo spectroscopy (ISIS). A new technique for spatially selective nmr spectroscopy. J. Magn. Reson. 1986; 66: 283–294.
37. McDaniel JR, Dewhirst MW, Chilkoti A. Actively targeting solid tumours with thermoresponsive drug delivery systems that respond to mild hyperthermia. Int. J. hyperthermia. Off J. Eur Soc. Hyperthermic Oncol. North Am. Hyperthermia Group 2013; 29: 501–510.
38. Sagiyama K, Mashimo T, Togao O, Vemireddy V, Hatanpaa KJ, Maher EA, Mickey BE, Pan E, Sherry AD, Bachoo RM, Takahashi M. In vivo chemical exchange saturation transfer imaging allows early detection of a therapeutic response in glioblastoma. Proc. Natl Acad. Sci. U. S. Am. 2014; 111(12): 4542–4547.
39. Chen LQ, Howison CM, Jeffery JJ, Robey IF, Kuo PH, Pagel MD. Evaluations of extracellular pH within in vivo tumors using acidoCEST MRI. Magn. Reson. Med. 2014; 72(5): 1408–1417.
40. Maritim S, Huang Y, Coman D, Hyder F. Characterization of a lanthanide complex encapsulated with MRI contrast agents into liposomes for biosensor imaging of redundant deviation in shifts (BIRDS). J. Biol. Inorg. Chem. 2014; 19(8): 1385–1398.
41. Hedaya MA, Elmquist WF, Sawchuk RJ. Probenecid inhibits the metabolic and renal clearances of zidovudine (AZT) in human volunteers. Pharm. Res. 1990; 7(4): 411–417.
42. Doblas S, He T, Saunders D, Hoyle J, Smith N, Pye Q, Lerner M, Jensen RL, Towner RA. In vivo characterization of several rodent glioma models by 1 H MRS. NMR Biomed. 2012; 25(4): 685–694.
43. Tropres I, Pannetier N, Grand S, Lemasson B, Moisan A, Peoc'h M, Remy C, Barbier EL. Imaging the microvessel caliber and density: Principles and applications of microvascular MRI. Magn. Reson. Med. 2014. DOI:10.1002/mrm.25396.
44. Wechsler W, Teske U, Reifenberger G, Deckert M, Seitz RJ, Mies G, Paschen W, Hossmann KA. Neuropathology and Regional Imaging of Microcirculation, Tissue pH, Metabolites and Necroses in Cerebral RG2 and F98 Anaplastic Rat Glioma Transplantation Tumors. In *Brain Oncology Biology, diagnosis and therapy*, Chatel M, Darcel F, Pecker J (eds). Volume 52. Developments in Oncology: Springer Netherlands, 1987; 187–199.
45. Estrella V, Chen T, Lloyd M, Wojtkowiak J, Cornnell HH, Ibrahim-Hashim A, Bailey K, Balagurunathan Y, Rothberg JM, Sloane BF,

Johnson J, Gatenby RA, Gillies RJ. Acidity generated by the tumor microenvironment drives local invasion. Cancer Res. 2013; 73(5): 1524–1535.
46. Garcia-Martin ML, Herigault G, Remy C, Farion R, Ballesteros P, Coles JA, Cerdan S, Ziegler A. Mapping extracellular pH in rat brain gliomas in vivo by 1 H magnetic resonance spectroscopic imaging: comparison with maps of metabolites. Cancer Res. 2001; 61(17): 6524–6531.
47. Sherry AD, Woods M. Chemical exchange saturation transfer contrast agents for magnetic resonance imaging. Annu. Rev. Biomed. Eng. 2008; 10: 391–411.
48. Harris RJ, Cloughesy TF, Liau LM, Prins RM, Antonios JP, Li D, Yong WH, Pope WB, Lai A., Nghiemphu PL, Ellingson BM. pH-weighted molecular imaging of gliomas using amine chemical exchange saturation transfer MRI. Neuro Oncol. 2015; 17(11): 1514–1524.
49. Evelhoch JL. pH and therapy of human cancers. Novartis Found. Symp. 2001; 240: 68–80 discussion 80–64, 152–153.
50. Gerweck LE, Richards B. Influence of pH on the thermal sensitivity of cultured human glioblastoma cells. Cancer Res. 1981; 41(3): 845–849.
51. McSheehy PM, Troy H, Kelland LR, Judson IR, Leach MO, Griffiths JR. Increased tumour extracellular pH induced by Bafilomycin A1 inhibits tumour growth and mitosis in vivo and alters 5-fluorouracil pharmacokinetics. Eur. J. Cancer 2003; 39(4): 532–540.
52. Robey IF, Baggett BK, Kirkpatrick ND, Roe DJ, Dosescu J, Sloane BF, Hashim AI, Morse DL, Raghunand N, Gatenby RA, Gillies RJ. Bicarbonate increases tumor pH and inhibits spontaneous metastases. Cancer Res. 2009; 69(6): 2260–2268.
53. Silva AS, Yunes JA, Gillies RJ, Gatenby RA. The potential role of systemic buffers in reducing intratumoral extracellular pH and acid-mediated invasion. Cancer Res. 2009; 69(6): 2677–2684.

SUPPORTING INFORMATION

Additional supporting information can be found in the online version of this article at the publisher's web site.